

*Annual Review of Analytical Chemistry*

# Advances in Surface Plasmon Resonance Imaging and Microscopy and Their Biological Applications

Markéta Bocková, Jiří Slabý, Tomáš Špringer,  
and Jiří Homola

Institute of Photonics and Electronics, Czech Academy of Sciences, 18251 Prague,  
Czech Republic; email: homola@ufe.cz

**ANNUAL  
REVIEWS CONNECT**

[www.annualreviews.org](http://www.annualreviews.org)

- Download figures
- Navigate cited references
- Keyword search
- Explore related articles
- Share via email or social media

Annu. Rev. Anal. Chem. 2019. 12:151–76

First published as a Review in Advance on  
March 1, 2019

The *Annual Review of Analytical Chemistry* is online at  
[anchem.annualreviews.org](http://anchem.annualreviews.org)

<https://doi.org/10.1146/annurev-anchem-061318-115106>

Copyright © 2019 by Annual Reviews.  
All rights reserved

## Keywords

surface plasmon, surface plasmon resonance, imaging, microscopy, optical biosensor, detection of biomolecules, biomolecular interaction analysis

## Abstract

Surface plasmon resonance microscopy and imaging are optical methods that enable observation and quantification of interactions of nano- and microscale objects near a metal surface in a temporally and spatially resolved manner. This review describes the principles of surface plasmon resonance microscopy and imaging and discusses recent advances in these methods, in particular, in optical platforms and functional coatings. In addition, the biological applications of these methods are reviewed. These include the detection of a broad variety of analytes (nucleic acids, proteins, bacteria), the investigation of biological systems (bacteria and cells), and biomolecular interactions (drug–receptor, protein–protein, protein–DNA, protein–cell).

## INTRODUCTION

Understanding how life works on the molecular and cellular levels is an important challenge for modern science. Addressing this challenge requires the development of sensitive and robust tools for the investigation of biomolecules, cells, and their interactions. Label-free affinity biosensors present an emerging technology that holds vast potential for these applications (1). Affinity biosensors based on optically excited surface plasmons represent the most advanced label-free optical affinity biosensor method. The first reports on the use of surface plasmons for probing processes on the surfaces of metal layers (2) and sensing (3) date back to the 1980s. In the early 1990s, the first surface plasmon-based biosensors [referred to as surface plasmon resonance (SPR) biosensors] were demonstrated and applied to the investigation of biomolecular interactions (4). In the following years, SPR biosensors have become an important tool with a significant impact on biophysics, molecular biology, and pharmaceutical research. Conventional SPR biosensors enable real-time observation and quantification of interactions between biological objects in a liquid sample and their counterparts immobilized on the surface of a metal supporting surface plasmons. In contrast to such biosensors that create the sensor output by integrating signals from the interactions occurring within macroscopic areas of the surface, SPR imaging and microscopy are methods that aim to allow localization of these interactions through the imaging of the metal surface by means of surface plasmons. The origins of SPR microscopy and imaging date back to the 1980s, when Yeatman & Ash (5) and Rothenhäusler & Knoll (6) reported the first spatially resolved plasmonic measurements. These pioneering studies have inspired a great deal of research, and numerous SPR imaging and microscopy platforms have been developed and applied to a multitude of biological problems. SPR imaging and microscopy have been subject to numerous publications, including several comprehensive reviews (7–13).

In this review, we explain the fundamentals of surface plasmon imaging and microscopy and discuss selected advances in the development and applications of these methods over the past five years. These include the detection of biomolecules and the investigation of biological systems and biomolecular interactions.

## PRINCIPLES OF SURFACE PLASMON RESONANCE IMAGING AND MICROSCOPY

Surface plasmon is a mode of electromagnetic field that is associated with collective oscillations of free conductive electrons in the metal near metal-dielectric interface. The electromagnetic field of the surface plasmon is localized to the interface and decays into both the metal and the dielectric. This characteristic makes surface plasmons an effective tool for probing processes on metal surfaces (14, 15). A wide variety of surface plasmon modes exist on different metal-dielectric (nano)structures (16).

Propagating surface plasmon (PSP) supported by a continuous metallic film is the surface plasmon mode most commonly used in SPR imaging and microscopy. The electromagnetism of PSP may be characterized by its penetration depth to the dielectric ( $\sim 10^2$  nm) and its propagation length ( $\sim 10^1$   $\mu$ m). Metal-dielectric multilayers may alter these characteristics, as demonstrated by the long-range and short-range surface plasmons propagating along a thin metal film embedded between two dielectrics (17). Localized surface plasmon (LSP) is supported by an individual metal nanoparticle. The electric field of a fundamental LSP mode oscillates as an electric dipole and exhibits a penetration depth on the order of tens to hundreds of nanometers. Other surface plasmons are supported by periodic arrays of metal nanoparticles. These modes originate from the coupling of light diffracted parallel to the surface (surface lattice resonances) with single-particle LSPs. These modes exhibit rather delocalized electromagnetic field (in comparison with

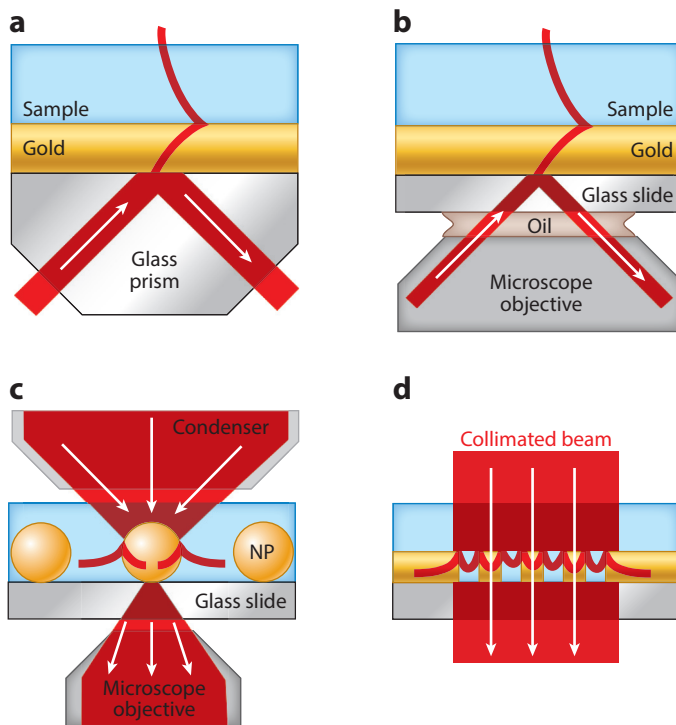


**Figure 1**

Optical excitation of surface plasmons: (a) a prism-based attenuated total reflection configuration for SPR imaging, (b) a high numerical aperture objective configuration for SPR microscopy, (c) transmission arrangement for localized SPR microscopy, and (d) a collinear transmission arrangement for SPR imaging. Abbreviations: NP, nanoparticle; SPR, surface plasmon resonance.

LSPs) and have a penetration depth on the order of hundreds of nanometers (18). Furthermore, surface plasmons originating from the interplay between various surface plasmons such as diffractively coupled PSPs and localized cavity modes may exist on a periodic array of nanoapertures in a metal film (19–22).

The main approaches to the optical excitation of surface plasmons are shown in **Figure 1**. The most widely used geometry is based on the attenuated total reflection (ATR) method and prism coupling (**Figure 1a**). The ATR configuration is typically used to excite surface plasmons such as PSPs on unstructured metal films. Incident light passes through a prism and is made incident on the base interfaced with a plasmonic structure under an angle of incidence larger than the critical angle, generating an evanescent wave. When the propagation constant of the wave is equal to that of surface plasmons on the plasmonic structure, the light excites the surface plasmons, which results in a decreased intensity of the reflected light. PSPs on an unstructured metal film can also be excited by light focused to the side of the back focal plane of a high numerical aperture oil immersion objective to illuminate a metal film with the use of collimated beam at the desired angle of incidence (**Figure 1b**). The reflected light from the metal film is collected by the same objective. Alternatively, surface plasmons on nanostructures (e.g., LSPs) can be excited and observed in a reflection or transmission microscope (**Figure 1c**). The illumination is adjusted to be either collimated or convergent, depending on the characteristics of the surface plasmon; furthermore, dark-field illumination through a dark-field condenser can be employed, and the scattered light can

be collected and analyzed. Other optical platforms are based on collinear geometry (**Figure 1d**). In this geometry, collimated light is made incident onto a plasmonic structure (periodic arrays of nanoparticles, nanoholes, nanoslits, randomly distributed nanoparticles) and excites surface plasmons while generating changes in the intensity of the reflected or transmitted light. Although the approach depicted in **Figure 1a** is often referred to as SPR imaging, and the approach depicted in **Figure 1b** is often referred to as SPR microscopy, this terminology is not used consistently in the literature. In this review, we use the term SPR imaging for all of the platforms in which the sensing surface (structured or unstructured) is illuminated by a rather large (and often collimated) beam of light and surface plasmons are excited by means of an ATR prism or diffraction couplers. Furthermore, we use the term SPR microscopy for all of the platforms in which a beam of light is focused onto a small area of the sensing surface (structured or unstructured) and surface plasmons are excited via a microscope objective.

## ADVANCES IN OPTICAL PLATFORMS

### Surface Plasmon Resonance Imaging and Prism-Based Platforms

The ATR method has been used in SPR imaging for over three decades, and numerous platforms based on this approach have been developed and even commercialized (23). Therefore, in recent years, attention has mainly focused on aspects affecting the performance of prism-based SPR imaging platforms.

Corso et al. (24) combined angle-resolved SPR and SPR imaging in one instrument, which allowed them to set the measurement conditions for SPR imaging that provide the best sensitivity. In addition, SPR imaging platforms were proposed that allow for the acquisition of the entire spectrum of light coupled to surface plasmons from each spot (spectral imaging). Shao et al. (25) developed a prism-based SPR two-dimensional (2D) spectral imaging sensor with phase interrogation. They used a liquid crystal tunable filter to vary the input wavelength and a liquid crystal modulator to introduce phase retardation between the s- and p-polarizations to create a platform enabling the measurement of phase retardation at multiple wavelengths. The sensor was demonstrated to attain a refractive index (RI) resolution as low as  $2.7 \times 10^{-7}$ . Subsequently, the same group developed an SPR imaging platform employing an acousto-optic tunable filter with an RI resolution of  $1 \times 10^{-6}$  (26). The factors limiting spatial resolution in prism-based SPR imaging were studied by Laplatine et al. (27), who showed that these platforms suffer from geometrical aberrations that can be even more limiting than the propagation length of surface plasmons. By optimizing the prism coupler and introducing the line-scan imaging mode, they demonstrated that lateral resolution can be improved down to 2.8  $\mu\text{m}$ .

### Surface Plasmon Resonance Imaging and Collinear Optics Platforms

Botazzi et al. (28) developed a compact optical platform using pillars buried in a gold film with an RI resolution of  $4 \times 10^{-6}$ . The same plasmonic structures were used in an even more compact platform ( $10 \times 15 \times 6 \text{ cm}^3$ ) with an RI resolution of  $6 \times 10^{-5}$  (22). Gomez-Cruz et al. (29) developed a fully integrated platform based on a nanohole array and achieved an RI resolution of  $10^{-6}$ . Guner et al. (30) reported an SPR imaging platform based on a smartphone and a disposable grating coupler that achieved an RI resolution of  $4 \times 10^{-5}$ . Lee et al. (31) developed an SPR imaging platform based on a smartphone LED and camera and capped nanoslit arrays. Each chip contained several arrays with different periods. The transmitted light was recorded, and the period producing the strongest coupling was determined and used as a sensor output.

Cappi et al. (32) developed an SPR imaging platform employing gold nanoislands. They used a white LED and a color CMOS detector to enable spectral measurement. By analyzing images from pixels with red, green, and blue filters of the detector, the spectral position of the LSPR peak was determined. A spectral SPR imaging platform based on a hybrid surface plasmon mode of a periodic array of nanoholes was developed by Guo & Guo (20). They detected the first diffraction order with a camera enabling the acquisition of the spectrum of light coupled to surface plasmons without the use of an additional dispersive element. Van Duyne's group (33) developed a spectral SPR imaging sensor utilizing a liquid crystal tunable filter. Light transmitted through an array of metal nanodiscs was passed through a liquid crystal-tunable filter and received by a detector to yield images at multiple wavelengths. An alternative spectral SPR imaging approach was developed by Lee et al. (34), who used a broadband light source and a tunable monochromator attached to a microscope. They measured the intensity of light transmitted through a nanoslit array and achieved an RI resolution of  $1 \times 10^{-5}$ .

### Surface Plasmon Resonance Microscopy

SPR microscopy platforms tend to exhibit better spatial resolution than their SPR imaging counterparts and are therefore the platform of choice when high spatial resolution is required. Spatial resolution for SPR microscopy platforms based on unstructured metal films is limited mainly by the propagating nature of surface plasmons, as their propagation length is usually much larger than diffraction-limited resolutions provided by high numerical aperture objectives ( $0.2 \mu\text{m}$  for an objective with a numerical aperture of 1.4 and a wavelength of 550 nm). Therefore, numerous studies were concerned with reducing the propagation length of surface plasmons. Banville et al. (35) demonstrated that the propagation length of surface plasmons can be reduced by the use of plasmonic nanostructures. They investigated the trade-off between the spatial resolution and image contrast and found that nanostructuring enables submicrometer spatial resolution. Banville et al. (36) also demonstrated a method to improve lateral resolution in SPR microscopy by combining images acquired with surface plasmons propagating in opposite directions. Kim's group (37) developed a similar approach by using a linear motor stage for spatially switching the direction of surface plasmon momentum. The resolution of the reported platform was almost 15 times better than that of conventional SPR microscopy. Another approach for improving the spatial resolution was developed by Somekh's group (38). They constructed a wide-field SPR microscope with angular scanning that employed an amplitude spatial light modulator placed in a conjugated back focal plane to allow for dynamic control of the illumination angle and collection of SPR images at different angles of incidence. The spatial resolution can also be improved by using a scanning approach proposed by Watanabe et al. (39), who used different SPR images generated while changing the position of the SPR chip. Argoul's group (40) has improved the scanning SPR microscope by reducing the readout area corresponding to a single detector pixel with radially polarized illumination and a fiber-based interferometer. They showed that the resolution of such a microscope reaches the theoretical diffraction limit.

Whereas most SPR microscopes gather only information about changes in the amplitude or phase of light coupled to surface plasmons, holographic approaches measure both of these quantities (41). Zhang et al. (42, 43) developed a compact SPR holographic microscope employing a Wollaston prism in which the p-polarized light (both amplitude and phase) that carried the information of interest was combined with reference s-polarized light; the resulting interferogram was used for SPR image reconstruction. Gao et al. (44) developed a platform based on an on-chip interferometer consisting of a slit and groove in a metallic film for monitoring the phase difference of surface plasmons propagating in between them. In addition, a design based on two

coupled interferometers was explored, and the resolution of the single-interferometer and double-interferometer sensors was  $3 \times 10^{-4}$  and  $5 \times 10^{-5}$ , respectively.

Another SPR microscopy platform was described by Chen et al. (45), who used dark-field illumination and an array of gold nanorods. The LSPs were excited by a light-passing condenser, and the scattered light was collected by a 10 $\times$  magnification objective. The authors compared their proposed approach with a similar spectrometry-based LSPR sensor and estimated that it provides a tenfold improvement in sensing performance.

Altug's group (19, 46) developed a 1D spectral SPR microscopy platform using three nanohole arrays in a row. Light from a broadband source was transmitted through the nanohole substrate mounted in an inverted microscope and analyzed by an imaging spectrometer. The optical spectrum for each array was acquired, and the spectral position of the LSPR peak was determined.

Liu et al. (47) developed a platform for the interrogation of individual nanoparticles in a dark-field SPR microscope. The light transmitted through a sparse array of nanospheres was made incident on a grating and diffracted onto a camera. The recorded image contained mutually shifted zero and first diffraction order images, and the first diffraction order was used to obtain the spectral position of the LSPR.

## ADVANCES IN FUNCTIONALIZATION METHODS

To fully exploit the potential of spatially resolved SPR imaging and microscopy methods, functionalization approaches are desired that can deliver biological functionality to plasmonic structures in a spatially resolved manner. The scale and spatial resolution vary broadly depending on the application, from immobilizing a multitude of different biomolecules into a large array (>100) of macroscopic (0.01 mm<sup>2</sup>) spots, to delivering a single-type biomolecule to individual nanoscopic plasmonic features. A detailed description of common immobilization methods can be found in books (15, 48) and reviews (49, 50). In this section, we focus on advances in the functionalization of arrays on macroscopic areas. For advances in spatially resolved functionalization of nanostructures, we refer the reader to our recent review (16). The primary focus is on methods for the preparation of protein and nucleic acid arrays; immobilization of bacteria is typically accomplished via specific receptors (antibodies or carbohydrates) covalently attached to surface carboxy-terminated self-assembled monolayers (51) or via receptor-pyrrole conjugates that are prepared by electrochemical polymerization (52).

Most functionalization methods used to produce bimolecular arrays are typically based on microspotting techniques (contact or noncontact printing, or microfluidics-, microstamping- or lithography-based approaches) (49). A method for the preparation of arrays of peptide nucleic acid (PNA) probes was proposed by Simon et al. (53). The method is based on direct microspotting of thiol-terminated PNA probes prehybridized with a short complementary DNA strand [instead of using single-stranded PNA (ssPNA) probes] that are subsequently removed by NaOH. This ensures optimal surface density and orientation of the PNA probes. The resulting PNA arrays were demonstrated to be superior (or equal) in terms of binding capacity to those obtained by standard ssPNA microspotting. Nand et al. (54) proposed an *in situ* protein synthesis method to generate protein arrays directly from prearrayed plasmid DNA probes, exploiting the high-affinity interaction between the protein TUS tag and the TER DNA sequence. A mixture of plasmid DNA and amine-terminated TER DNA was microspotted on a sensor surface functionalized with polyethyleneimine; *in vitro* transcription and translation (IVTT) mix was added, and fusion proteins were synthesized. The feasibility of the method was demonstrated in experiments with the binding of protein-specific antibodies. A two-step templated, ribosomal biosynthesis-based printing method for the fabrication of protein microarrays was reported by Manuel et al. (55). In

the first step, a microarray of proteins was created in microwells by cell-free protein synthesis; each microwell contained both an IVTT mix and a specific DNA template sequence that were used together to create specific hexahistidine-tagged proteins. In the second step, the protein microwell array was used to contact print the protein microarray onto a nitrilotriacetic acid-functionalized SPR imaging chip. Another method for the preparation of proteins arrays was proposed by Kruis et al. (56), who utilized leucine zipper heterodimerization. The sensor surface was functionalized with thiol-terminated zwitterionic peptides, a small percentage of which carried leucine zipper moiety. Using a continuous flow microspotter, proteins with the complementary leucine zipper fusion tag were immobilized to create a protein array.

Wood et al. (57) used a polydopamine (PDA) multilayer for the fabrication of DNA microarrays. Dopamine monomers self-polymerize to create a PDA layer on gold that enables the covalent attachment of biomolecules via amine coupling. In this work, PDA multilayers were formed on gold spots through repeated injections of dopamine, after which amine-terminated DNA probes were attached.

## BIOANALYTICAL APPLICATIONS

In this section, we review bioanalytical applications of SPR imaging and microscopy. The main characteristics of these applications are presented in **Table 1**.

### Detection of Protein Biomarkers

C-reactive protein (CRP), a clinical biomarker of acute inflammatory diseases, was targeted by Altug's group (58). The authors used a brightfield SPR imaging sensor based on an array of gold nanoholes (see **Figure 2**) that allowed for the visualization of individual gold nanoparticles (AuNPs) captured on the surface of the array. The surface of the chip was functionalized with anti-CRP antibodies, and a sandwich assay with antibody-coated 100-nm AuNPs was used to detect CRP. The authors detected CRP down to 27 and 100 pg/mL in buffer and cell culture media with 10% horse serum, respectively.

An ovarian cancer marker, protein r-PAX8, was detected by Escobedo et al. (59) using a nanohole array-based platform. The sensor surface was functionalized with anti-r-PAX8 antibody via amino coupling, and protein r-PAX8 was detected in buffer at concentrations down to 0.25 µg/mL.

Hu et al. (60) used SPR imaging to detect the tumor marker  $\alpha$ -fetoprotein. The sensing surface was functionalized with the poly[oligo(ethylene glycol) methacrylate-co-glycidyl methacrylate] (POEGMA-co-GMA) brush and an anti- $\alpha$ -fetoprotein antibody. A two-step sandwich assay with functionalized AuNPs was employed, and  $\alpha$ -fetoprotein was detected in 10% human serum with a limit of detection (LOD) of 1 ng/mL.

Moreover, Hu et al. (61) detected a colorectal cancer biomarker, carcinoembryonic antigen (CEA), using SPR imaging, POEGMA-co-GMA functional coating, and a two-step sandwich assay where the sensor response was enhanced by an antibody-modified PDA reduced graphene oxide (PDA-rGO) followed by a PDA-induced spontaneous reductive deposition of gold on PDA-rGO. CEA was detected in 10% human serum with an LOD of 500 pg/mL. CEA was also targeted by Liu et al. (62). The surface of an SPR imaging sensor was microspotted with thiol-terminated aptamers against CEA, which was detected using a multistep sandwich assay in which the capture of CEA by aptamer was followed with repeated injections of concanavalin A and dextran to enhance the sensor response. CEA concentrations as low as 50 pg/mL were detected in both buffer and 10% human serum sample.



**Table 1** Selected examples of applications of plasmonic biosensors for the detection of chemical and biological species

| Target   | Detection format<br>(detection time)                  | Performance <sup>a</sup>   | Optical platform   | Reference |
|--|---|--|--|-----------|
| <b>Protein biomarkers</b>                      |   |  |  |           |
| CRP  | SA: Ab–AuNP (2 h)                                     | LOC: 27 pg/mL<br>LOC: 100 pg/mL,<br>10% horse serum                          | Collinear using gold<br>nanohole array                       | 58        |
| r-PAX8   | Direct detection (15 min)                             | LOC: 0.25 µg/mL  | Collinear using gold<br>nanohole array                       | 59        |
| AFP  | 2-Step SA: Ab–AuNP +<br>polymerization (2.5 h)        | LOD: 1 ng/mL,<br>10% human serum   | Prism-based using<br>gold film                               | 60        |
| CEA  | 2-Step SA:<br>Ab–PDA-rGO + gold<br>deposition (2.5 h) | LOD: 0.5 ng/mL,<br>10% human serum   | Prism-based using<br>gold film                               | 61        |
| CEA  | Multistep SA: concavalin<br>A + dextran (>1 h)        | LOC: 50 pg/mL,<br>10% human serum  | Prism-based using<br>gold film                               | 62        |
| HER2   | Direct detection (1 h)                                | LOC: 3 ng/mL   | Collinear using<br>nanoholes                                 | 63        |
| PTX3   | Direct detection (1 min)                              | LOC: 100 ng/mL   | Collinear using buried<br>nanoholes                          | 28        |
| CatG   | Direct detection (10 min)                             | LOD: 0.23 ng/mL  | Prism-based using<br>gold film                               | 64        |
| CatG   | Direct detection (10 min)                             | LOC: 0.9 pmol/mL,<br>2% endometrial tissue                                   | Prism-based using<br>gold film                               | 65        |
| Laminin-5                                      | Direct detection (10 min)                             | LOD: 4 pg/mL<br>LOC: 37 ng/mL,<br>0.1% human plasma                          | Prism-based using<br>gold film                               | 66        |
| Collagen IV                                    | Direct detection (10 min)                             | LOD: 2,400 pg/mL<br>LOC: 50 ng/mL,<br>10% human plasma                       | Prism-based using<br>gold film                               | 67        |
| Metalloproteinase-1                            | Direct detection (10 min)                             | LOD: 9 pg/mL<br>LOD: 3 ng/mL, human<br>plasma                                | Prism-based using<br>gold film                               | 68        |
| IL-1 β, IL-6, IFN-γ, and<br>TNF-α              | SA: biotin–AuNP (3 h)                                 | LOD: 1.2, 0.05, 22, and<br>15 pg/mL  | Prism-based using<br>gold film                               | 69        |
| IL-2, IL-4, IL-6, IL-10,<br>IFN-γ, TNF-α       | Direct detection (40 min)                             | LOD: 5–20 pg/mL<br>LOC: 32 pg/mL, human<br>serum                             | Dark-field microscopy<br>of nanorods                         | 45        |
| IL-2, IFN-γ, TNF-α,<br>IL-10                   | Direct detection (30 min)                             | LOD: 21–35 pg/mL   | Dark-field microscopy<br>of nanorods                         | 70        |
| <b>Other proteins</b>                          |   |  |  |           |
| Thrombin, IgE,<br>streptavidin,<br>fibronectin | Direct detection (45 min)                             | LOD: 1 nM (60 ng/mL) for<br>streptavidin                                     | Dark-field microscope<br>using nanorods,<br>spectral imaging | 71        |
| <b>Nucleic acids with medical relevance</b>    |   |  |  |           |
| miR-15a  | SA: ON +<br>polymerization (2.5 h)                    | LOD: 0.5 fM (~2.5 fg/mL)<br>LOC: 3.5 fM<br>(~17.5 fg/mL), 40%<br>human serum | Prism-based using<br>gold film                               | 72        |

(Continued)

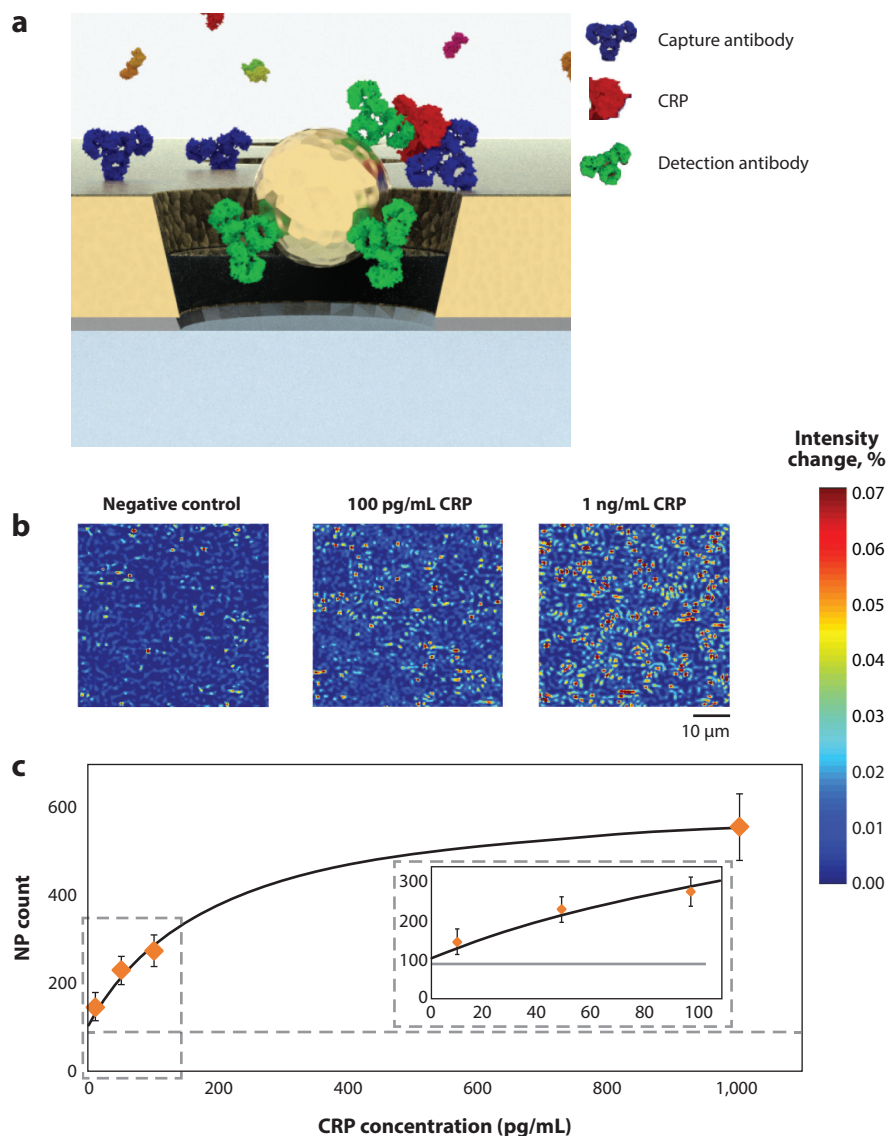


Table 1 (Continued)

| Target   | Detection format (detection time) | Performance <sup>a</sup>   | Optical platform                                   | Reference |
|--|-----------------------------------|--|--|-----------|
| miR-16, miR-181, miR-34a, miR-125b   | SA: strep–AuNP (35 min)           | LOD: 0.35, 0.39, 0.5, 0.95 pM (~2, 2, 3, 5 pg/mL), 90% erythrocyte lysate samples    | Prism-based using gold film                        | 73        |
| ON <i>ABCB1</i> gene   | Direct detection (6 min)          | LOD: 0.5 nM (~2.5 ng/mL)   | Prism-based using gold film                        | 74        |
| <i>BCR/ABL</i> fusion gene   | Direct detection (20 min)         | LOD: 10 nM (~100 ng/mL)  | Prism-based using gold film                        | 75        |
| <b>Bacterial nucleic acids</b>   |                                   |  |  |           |
| 16S RNA ( <i>Legionella pneumophila</i> )  | SA: strep–quantum dots (3 h)      | LOD: 1 pM (~10 pg/mL)  | Prism-based using gold film                        | 76        |
| 16S RNA: <i>L. pneumophila</i>   | SA: ON–AuNP (1 h)                 | LOD: 1 pM (~10 pg/mL)  | Prism-based using gold film                        | 77        |
| 16S RNA: <i>L. pneumophila</i> , <i>Pseudomonas aeruginosa</i> , <i>Salmonella typhimurium</i> | SA: ON–AuNP (0.5 h)               | LOC: 10 pg/mL (all three strains)  | Prism-based using gold film                        | 78        |
| Genomic DNA ( <i>Staphylococcus aureus</i> )   | SA: ON–AuNP (T > 30 min)          | LOC: 1 fM (~10 fg/mL)  | Prism-based using gold film                        | 79        |
| <b>Bacteria</b>  |                                   |  |  |           |
| <i>Salmonella enteritidis</i> , <i>S. pneumoniae</i> , <i>Escherichia coli</i> O157:H7         | Direct detection (<7 h), CCM      | LOC: 3 CFU/mL, culture medium<br>LOC: 60 CFU/mL, 10% milk, mineral water, ground bee | Prism-based using gold film                        | 80        |
| <i>E. coli</i> O157:H7   | Direct detection (<10 h), CCM     | LOC: 100 CFU/mL, culture medium  | Prism-based using gold film                        | 52        |
| <i>E. coli</i> O157:H7   | Direct detection (<10 h), CCM     | LOC: 10 CFU/mL, culture medium   | Prism-based using gold film                        | 81        |
| <i>Cronobacter</i> spp., <i>Salmonella</i> spp.  | Direct detection (<24 h), CCM     | LOC: 30 CFU/25 g, powdered infant formula  | Prism-based using gold film                        | 82        |
| <i>Chlamydia trachomatis</i> , <i>Neisseria gonorrhoeae</i>                                    | Direct detection (10 min)         | LOD: 300 CFU/mL<br>LOD: 1,500 CFU/mL   | Collinear system using nanoholes, spectral imaging | 46        |
| <i>Candida albicans</i>  | SA: Ab (1 h)                      | LOD: 10 <sup>6</sup> cells/mL  | Prism-based using gold film                        | 83        |
| <b>Bioparticles</b>  |                                   |  |  |           |
| IAV, HIV-VLP   | Direct detection (~seconds)       | LOC: 10 <sup>9</sup> /mL   | Prism-based using gold film                        | 84        |
| Exosomes   | Direct detection (10 min)         | LOC: 5 µg/mL   | Prism-based using gold film                        | 85        |

<sup>a</sup>Determined in buffer unless otherwise stated.

Abbreviations: Ab, antibody; AFP,  $\alpha$ -fetoprotein; AuNP, gold nanoparticle; CatG, cathepsin G; CCM, culture/capture/measure approach; CEA, carcinoembryonic antigen; CRP, C-reactive protein; HER2, human epidermal growth factor receptor type 2; HIV-VLP, human immunodeficiency virus-based virus-like particles; IAV, inactivated influenza A virus; IFN- $\gamma$ , interferon-gamma; IgE, immunoglobulin E; IL, interleukin; LOC, lowest observed concentration; LOD, limit of detection; ON, oligonucleotide; PDA, polydopamine; PTX3, pentraxin 3; rGO, reduced graphene oxide; SA, sandwich assay; Strep, streptavidin; TNF- $\alpha$ , tumor necrosis factor- $\alpha$ .



**Figure 2**

AuNP-enhanced detection of CRP using a surface with nanoholes. (a) CRP sandwich assay. (b) Different concentrations of CRP visually distinguished on surface plasmon resonance imaging. (c) Calibration curve for CRP. All panels adapted with permission from Reference 58. Copyright 2018 American Chemical Society. Abbreviations: AuNP, gold nanoparticle; CRP, C-reactive protein.

A breast cancer biomarker, human epidermal growth factor receptor 2 (HER2) antigen, was detected by Monteiro et al. (63). They used an SPR imaging platform based on an array of nanoholes functionalized with biotinylated anti-HER2 antibody attached via the immobilized streptavidin. The platform was demonstrated to directly detect HER2 in buffer at a concentration of 3 ng/mL.

Bottazzi et al. (28) developed an SPR imaging platform for the detection of pentraxin 3 (PTX3), a prospective biomarker of cardiovascular diseases and kidney pathologies. The platform was based

on a hexagonal lattice of polymeric pillars embedded in gold film to which anti-PTX3 was attached via amino coupling. Direct detection of PTX3 at concentrations of 100 ng/mL in buffer was achieved.

Cathepsin G (CatG), a molecule associated with an early immune response, was also targeted by the SPR imaging method (64, 65). The sensing spots were functionalized with MARS-115, a synthetic CatG inhibitor. Gorodkiewicz et al. (64) demonstrated the direct detection of CatG in buffer with an LOD of 0.23 ng/mL. In a subsequent study, the platform was applied to study endometriosis (65), and it was found that the CatG levels of patients suffering from this condition were twice as high as the control group. The same group also targeted other prospective cancer biomarkers, such as laminin-5, collagen IV, and metalloproteinase-1 (66–68), using the above-described methodology. In their study, laminin-5, collagen IV, and metalloproteinase-1 were directly detected in buffer with LODs of 4 (66), 2,400 (67), and 9 pg/mL (68), respectively. An analysis of clinical blood samples using SPR imaging revealed that patients with bladder and breast cancer exhibited higher concentrations of laminin-5 (66) and collagen IV (67), respectively.

Detection of cytokines using prism-based SPR imaging and specific antibodies was carried out by Kaiperien's group (69). Detection of selected cytokines, e.g., interleukin (IL)-1 $\beta$ , IL-6, interferon-gamma (IFN- $\gamma$ ), and tumor-necrosis-factor alpha (TNF- $\alpha$ ), was performed in a three-step sandwich assay with a biotinylated antibody, neutravidin, and biotinylated AuNPs. LODs of 1.2, 0.05, 22, and 15 pg/mL were claimed for IL-1 $\beta$ , IL-6, IFN- $\gamma$ , and TNF- $\alpha$ , respectively. Detection of 6 cytokines (IL-2, IL-4, IL-6, IL-10, IFN- $\gamma$ , and TNF- $\alpha$ ), was performed by Kurabayashi's group (45). They used dark-field LSPR imaging on a sparse array of antibody-coated nanorods. Cytokines were detected in buffer (LODs from 5 to 20 pg/mL) and then in undiluted human serum. In addition, the same group investigated the immunosuppressive drug-altered secretion of cytokines (IL-2, IFN- $\gamma$ , TNF- $\alpha$ , and IL-10) by T cells (70). Initially, Jurkat T cells were activated with a mixture of ionomycin and phorbol 12-myristate 13-acetate, and then the tacrolimus immunosuppressant was added. Using the assay described elsewhere (45), the secretion of all cytokines was measured in buffer with LODs of 21–35 pg/mL.

## Detection of Other Proteins

Multiplexed detection of four protein targets (thrombin, immunoglobulin E, streptavidin, and fibronectin) by dark-field SPR imaging was performed by Rosman et al. (71). The authors used four batches of nanorods, one for each protein, functionalized with their respective aptamers. Nanorods were sequentially injected over the sensor surface, and the position of each adsorbed nanorod was recorded. During the direct detection of proteins, the spatially resolved signal was matched with the map of aptamer-functionalized nanorods to determine the type of protein captured. LOD (1 nM) was only reported in the case of streptavidin.

## Detection of Nucleic Acids with Medical Relevance

MicroRNA miR-15a, a colon cancer biomarker, was detected by Hu et al. (72). They used gold islands functionalized with hairpin-structured thiolated DNA probes and a two-step enhancement strategy based on a sandwich assay combining (a) multiple binding of secondary oligonucleotides to the hairpin-structured probes that were previously opened by single miR-15a and (b) prolongation of a secondary oligonucleotide by *in situ* DNA-initiated polymerization. This approach achieved an LOD for miR-15a as low as 0.5 fM. Detection of miR-15a in 40% serum

obtained from healthy controls and patients with colon cancer was also performed, and concentrations of 10.5 and 3.5 fM were detected, respectively. Four microRNAs (miR-16, miR-181, miR-34a, and miR-125b), potential biomarkers of myelodysplastic syndrome, were targeted by Homola's group (73). A prism-based SPR imaging sensor was functionalized with ultralow fouling poly(carboxybetaine acrylamide) brushes to which DNA probes were covalently attached. Detection of microRNA was performed by means of a sandwich assay with streptavidin-coated AuNPs. The LODs ranging from 0.35 pM to 0.95 pM were established for microRNAs spiked in 90% erythrocyte lysate. Mariani et al. (74) used SPR imaging to detect an oligonucleotide sequence related to the single nucleotide polymorphism of the human *ABCB1* gene. They used SPR chips with different nanostructures that were functionalized with thiolated oligonucleotide probes. A nanostructure based on silver nanoprisms was found to be most sensitive, and the target oligonucleotide was detected directly with an LOD of 0.5 nM. The sequence of the *BCR/ABL* fusion gene, which plays a crucial role in the evolution of chronic myelogenous leukemia, was detected using prism-based SPR imaging by Wu et al. (75). The total RNA was extracted from K562 cells, and cDNA was obtained by applying a reverse transcription. The target DNA sequence was detected using an SPR chip functionalized with thiolated DNA probes, and an LOD of 10 nM was attained.

### Detection of Bacterial Nucleic Acids

Tabrizian's group (76, 77) reported on the use of SPR imaging for the detection of 16S rRNA from *Legionella pneumophila*. In the first report, they used an SPR chip functionalized with thiolated DNA probes and a sandwich assay with biotinylated secondary DNA probes and streptavidin-coated quantum dots (76) or a sandwich assay with oligonucleotide modified AuNPs (77). RNA from *L. pneumophila* was extracted and fragmented to obtain 16S rRNA. The same LOD of 1 pM was reported for both assays. The same group also demonstrated the simultaneous detection of 16S rRNA of three pathogenic bacterial strains: *L. pneumophila*, *Pseudomonas aeruginosa*, and *Salmonella typhimurium* using a sandwich assay with oligonucleotide-AuNPs (78). 16S rRNA at concentrations as low as 10 pg/mL was measured for all three strains. The detection of genomic DNA from *Staphylococcus aureus* was reported by Spoto's group (79) using an SPR chip functionalized with peptide nucleic acid probes and a sandwich assay with oligonucleotide-AuNPs. Genomic DNA concentrations down to 1 fM were detected.

### Detection of Bacteria

Pathogenic bacteria, such as *Salmonella enterica*, *Streptococcus pneumoniae*, *Escherichia coli* and *Cronobacter* spp., have been targeted by the research groups of Livache and Roupioz (52, 80–82). To detect extremely low levels of bacteria, they incorporated bacteria cultivation on an SPR chip, allowing for the detection of a greater population of cells [this is referred to as the culture/capture/measure (CCM) approach]. They used a prism-based SPR imaging platform functionalized with specific receptors (antibodies or carbohydrates). Using this approach, Bouguelia et al. (80) detected *Salmonella enteritidis*, *S. pneumoniae*, and *E. coli* O157:H7 in the buffer at concentrations as low as 3 CFU/mL. Mondani et al. (81) reported detection of *E. coli* O157:H7 at levels below 10 CFU/mL in 10% milk, mineral water, and ground beef samples cultivated on an SPR chip. Moreover, detection of *E. coli* O157:H7 in spring water and tap water, apple peel, and green salad was demonstrated with a similar detection performance (81). Proof-of-concept detection of *Cronobacter* spp. and *Salmonella* spp. was reported by Morlay et al. (82). They used an array of antibodies and demonstrated detection of both at levels down to 30 CFU in 25 g of powdered infant formula. Bulard et al. (52) used the CCM approach and

an array of carbohydrates immobilized on an SPR imaging chip to monitor their interaction with five different *E. coli* strains. They showed that the bacterial strains interacted differently with immobilized carbohydrates, providing a “carbohydrate binding fingerprint.” Using this platform, they detected and discriminated *E. coli* strains initially occurring at  $10^2$  CFU/mL levels.

*Chlamydia trachomatis* and *Neisseria gonorrhoeae*, which cause sexually transmitted infections, were detected using spectral SPR imaging with an array of nanoholes (46). The antibodies were captured on the surface of nanoholes via protein A/G. Bacteria were directly detected in buffer with LODs of 300 and 1,500 CFU/mL for *C. trachomatis* and *N. gonorrhoeae*, respectively.

Detection of *Candida albicans*, an opportunistic pathogenic yeast present in oral cavities, was detected using prism-based SPR imaging (83). The gold surface was functionalized with primary antibodies against *C. albicans* via amino coupling. The sandwich assay with antibodies was able to detect *C. albicans* in buffer with an LOD of  $10^6$  cells/mL.

## Detection of Bioparticles

Individual biological submicrometer-size objects such as spherically shaped viruses [inactivated influenza A virus (IAV)] and virus-like particles [human immunodeficiency virus-based virus-like particles (HIV-VLP)] were detected by Shpacovitch and coworkers (84). They used a prism-based SPR imaging platform functionalized with mucins (via thiol groups of cysteine-rich regions on mucin) or biotinylated antibodies (via biotin to the immobilized streptavidin) to capture IAV and HIV-VLP, respectively. The binding of individual IAV and HIV-VLP was observed in buffer; the binding of HIV-VLP was also observed in serum.

Tumor-derived exosomes were detected by Zhu et al. (85). They used prism-based SPR imaging and antibodies against transmembrane proteins CD9, CD63, CD82, CD41b, EpCAM, and E-cadherin that were spotted on the surface of an SPR chip. Exosomes isolated from human hepatocellular carcinoma cell lines (MHCC97L, MHCC97H) and mouse melanoma cell lines (B16-F1, B16-F10) were detected directly, and the method was able to detect exosome from the MHCC97H cell line at a concentration of 5  $\mu$ g/mL. It was also shown that highly metastatic cell lines (MHCC97H, B16-F10) secreted more exosomes than those with low metastatic effect (MHCC97L, B16-F1).

## INVESTIGATION OF BIOLOGICAL SYSTEMS

### Investigation of Bacteria

Tao's group (86) used SPR microscopy to monitor interactions of antibodies with individual bacteria. *E. coli* O157:H7 bacteria were attached to the sensor via covalently immobilized antibodies, and the interaction between the bacteria and the same antibodies contained in buffer was measured. The work demonstrates the feasibility of SPR microscopy-based analysis of biomolecular interactions involving single live bacteria and the effect of heterogeneity in a microbial population on these interactions. Tao's group also utilized SPR microscopy to quantify the motion of single bacteria and explored the correlation between this motion (resulting in changes in the image contrast) and antibiotic action on the bacterial metabolism (51). In this work, they studied *E. coli* O157:H7 interacting with a bactericidal antibiotic polymyxin B. The experiments revealed that antibiotic action significantly slows down bacterial motion.

Goluch's group (87) exploited SPR imaging to study bacterial films. In their earlier work they employed prism-based SPR imaging to monitor *E. coli* and *P. aeruginosa* that moved and attached across the sensor surface. Bacteria were placed in a growth medium on an SPR chip,

and the bacterial growth and biofilm formation were monitored in real time. Subsequently, they evaluated the efficacy of bovine serum albumin (BSA), casein, and penicillin/streptomycin surface coatings to prevent adhesion of *P. aeruginosa* and *S. aureus* (88). Prior to each experiment, protein and antibiotic solutions were pipetted to the SPR surface and left to dry. It was observed that bacterial attachment was most effectively inhibited by casein for both *P. aeruginosa* and *S. aureus*.

Mallevre et al. (89) used a prism-based SPR imaging sensor with the CCM approach to evaluate the toxicity of silver nanoparticles (AgNPs) and AgNO<sub>3</sub> on *S. enteritidis*. The dose-dependent changes in multiplication of the bacteria were consistent with those obtained by using a standard plating method. It was also shown that the toxic effect already occurs at mg/L levels.

## Investigation of Cells

Investigation of living adherent cells using a high-resolution scanning SPR microscope was reported by Argoul's group (90). They studied C2C12 mouse myoblast cells cultured on an SPR chip with respect to their adherence and motility. The evolution in shape of the adherent cells was tracked, and local dynamics of filopodia and lamellipodia protrusions was observed. Subsequently, they also observed the cellular migration, adhesion, detachment, and attachment of C2C12 mouse myoblast cells on the gold substrate (40). The process of the attachment of individual cells was studied by Tu et al. (91). They used SPR microscopy on a nanohole array interfaced with microfluidics incorporating single-cell trapping units. Mouse embryonic stem cells (C3H10) and human tumor cells (HeLa) were monitored during culturing, and it was demonstrated that the single-cell attachment process follows the logistic retarded growth model (with different parameters for the different cells).

A study of the transport of mitochondria along primary rat hippocampus neurons was carried out by Tao's group (92). They used an SPR microscope with advanced image postprocessing to track moving objects (localization precision  $\sim 5$  nm). Spatiotemporal measurements of neural cells seeded on a poly-L-lysine-coated SPR chip allowed for the tracking of mitochondria and determining the structure of microtubule bundles in neural cells.

As many intracellular signal transduction processes involve the remodeling of cytoskeleton or the translocation of signaling molecules, several attempts have been made to monitor cell response to various stimulations or to the spatial distribution of specific subcellular structures. Shinohara et al. (93) used prism-based SPR imaging to monitor intracellular signal transduction by translocation of protein kinase C (PKC). PC12 cells were cultured on an SPR chip and stimulated with K<sup>+</sup> or PKC activator phorbol-12-myristate-13-acetate (PMA) to induce PKC translocation that generated a sensor response. It was shown that cellular response to both K<sup>+</sup> and PMA increased with the concentration. The translocation of PKC was employed by Mir & Shinohara (94) who used prism-based SPR imaging to examine differentiation of PC12 cells on a poly-L-lysine-coated SPR chip. They demonstrated that their method can distinguish differentiated cells from nondifferentiated cells by comparing the sensor response to acetylcholine receptor agonists.

Zhang et al. (95, 96) used a prism-based SPR imaging method to investigate the response of living cells to various stimuli. Initially, they studied human type II alveolar epithelial cell line A549 cells cultured on an SPR chip that were stimulated by K<sup>+</sup> and epidermal growth factor (EGF). They demonstrated that the two different stimulants generated different sensor responses (95). Subsequently, they applied the same approach to analyze the response of a human hepatocellular carcinoma cell (HCC-LM3) to stimulation by K<sup>+</sup>, EGF, and vascular EGF (VEGF) (96). The



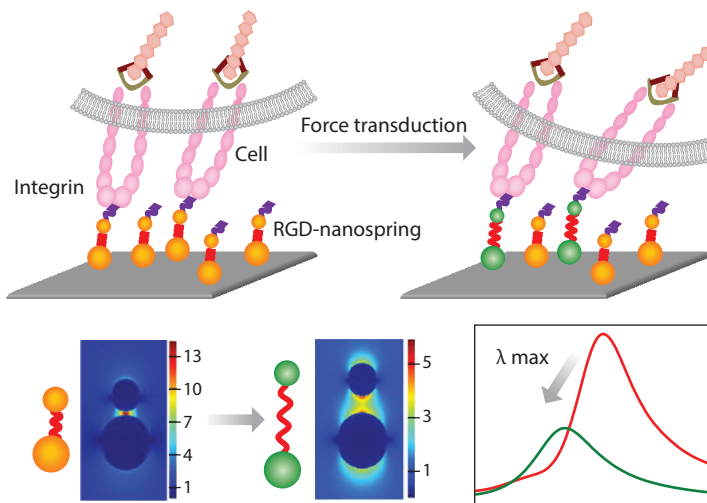


**Figure 3**

Schematic illustration for imaging mechanical force transduction with plasmonic nanosprings. Adapted with permission from Reference 98. Copyright 2017, American Chemical Society. Abbreviation: RGD, arginine–glycine–aspartic acid.

higher the concentration of  $K^+$ , the larger was the change in the sensor response. In contrast to EGF, VEGF did not produce any sensor response.

Tao's group (97) investigated the expression of EGF receptor (EGFR) and measured the kinetics of the binding of the antibody to EGFR on the cell surface with single-cell resolution. In this study, EGFR-overexpressed cells were grown on a collagen-coated SPR chip, and a monoclonal antibody (anti-EGFR) was used as a model to study the binding kinetics and affinity. The equilibrium dissociation constant was determined and shown to vary substantially from cell to cell. Experiments with cell lines having different EGFR-expression levels (A431, HeLa, and A549) showed that the steric hindrance effects of other membrane proteins may influence the drug–receptor interactions.

Xiong et al. (98) proposed an approach for the investigation of mechanical signals associated with mechanical forces propagating in cells. This approach is based on the combination of single-particle dark-field spectral microscopy and plasmonic nanosprings [two AuNPs connected by a polyethylene glycol (PEG) chain] that act as a mechanical sensor transferring force-induced molecular extension/compression to the optical response. The nanosprings used in this work consisted of AuNPs attached to the thiol-modified surface via Au–S chemistry and one smaller AuNP bound to the cell surface via RGD tripeptide–integrin interaction. Initially, the authors determined the relationship between the position of the spectral peak of one nanospring and the coupling distance, which was then correlated with the mechanical force exerted (**Figure 3**). This approach allowed for the visualization of the activation of localized mechanical force transduction in single live cells triggered by reactive oxygen species.

Berthuy et al. (99) tackled the problem of cell secretion by using prism-based SPR imaging. They employed human prostatic carcinoma cells (LNCaP) that were attached to an array of antibodies (anti-PSA, anti-B2M) microspotted on the sensor surface and monitored the secretion of PSA and B2M triggered by dihydrotestosterone by capturing the secreted PSA and B2M by the respective antibodies. Detection of antic-myc antibody secreted by an individual cell (9E10 hybridoma) attached to an array of nanodiscs was demonstrated by Raphael's group (100).



## INVESTIGATION OF MOLECULAR INTERACTIONS

### Drug–Protein Receptor Interactions

Li et al. (101) used prism-based SPR imaging to investigate the interaction between an immuno-suppressive drug (FK506) and its target protein (FKBP12). The calibration curve for the binding of FK506 to the immobilized FKBP12 protein was established and used to determine the equilibrium rate constant of the interaction. Subsequently, Zhou et al. (102) further studied FK506. This involved a drug–target recognition study on a protein mutation microarray (the interaction of FK506 with FKBP12 WT and six mutants arrayed on the surface), a drug-mediated protein–protein interaction study (the formation of conditioned FKBP12–FK506–calcineurin complex), and a multiplexed drug binding specificity study on a protein microarray (FK506, SB203580, and biotin-specific binding to FKBP12, p38- $\alpha$ , and streptavidin).

### Protein–DNA Interactions

Pillet et al. (103) used prism-based SPR imaging and dendrimeric functional coating to investigate the DNA–protein interaction model involved in *E. coli* plasmid segregation. They used five different amine-terminated DNA probes with different affinities to the SopB protein and determined the kinetic constants of their interactions with SopB. O’Sullivan’s group (104) used prism-based SPR imaging to monitor the interaction between protein and different thiol-modified aptamers chemisorbed on sensor surface. They determined the equilibrium dissociation constants of the interactions among these  $\beta$ -conglutin binding aptamers to be 20 nM, 13 nM, and 1 nM for  $\beta$ -CBA I,  $\beta$ -CBA II, and 11-mer, respectively.

### Protein–Protein Interactions

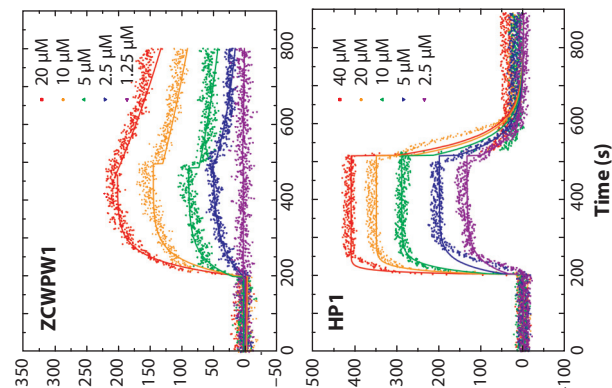
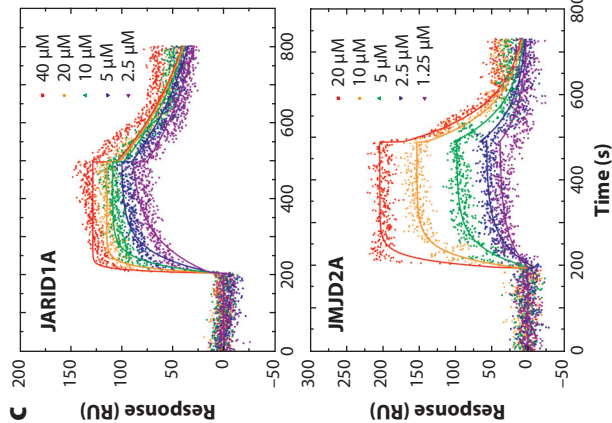
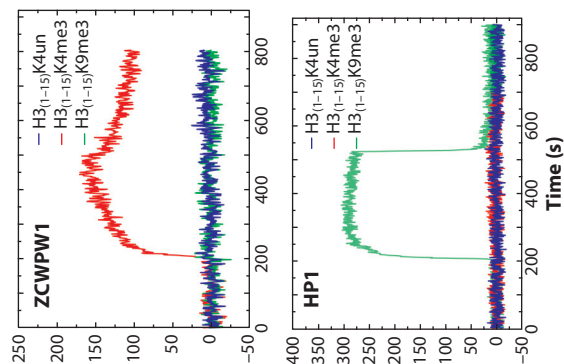
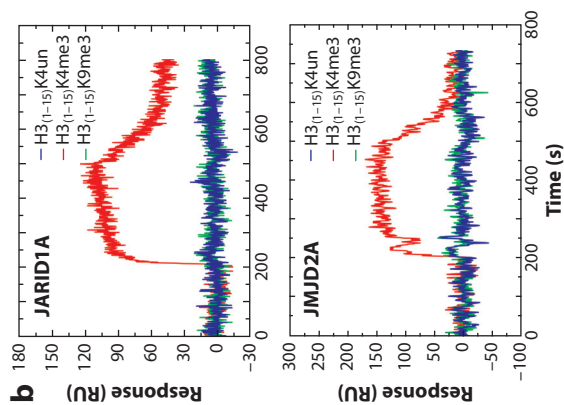
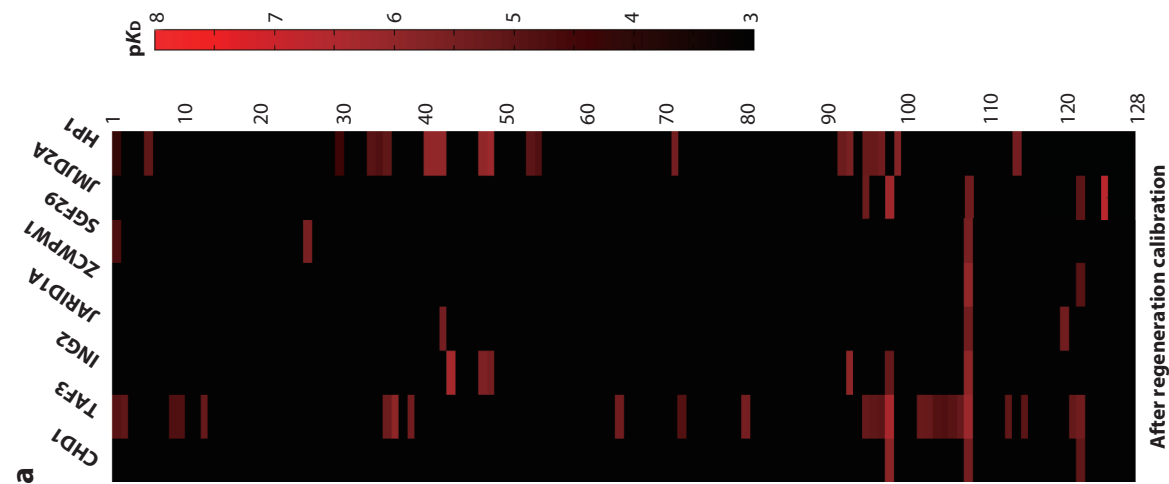
Miyachi et al. (105) used SPR imaging to investigate the binding of basic fibroblast growth factor 2 (FGF-2) to chondroitin sulfate (CS) tetrasaccharide conjugates. They found that the binding affinity of the CS tetrasaccharide structures to FGF-2 differed significantly, depending on whether they had a CS-E unit or a CS-D unit at the saccharide nonreducing end.

A nanoparticle-based SPR spectral imaging system was used for the analysis of carbohydrate–protein interactions (47). Bare AuNPs were attached to the glass substrate, functionalized with proteins (antitransferrin, antithrombin, BSA), and incubated with solutions containing carbohydrates (transferrin, heparin). Equilibrium binding constants of the interactions were extracted from the obtained calibration curves.

Zhao et al. (106) used prism-based SPR imaging for qualitative high-throughput profiling of epigenetic interactions between histone peptides and histone reader proteins. Selected 125 histone peptides were immobilized on the sensor surface, and their interactions with eight different proteins were analyzed in a single experiment to obtain respective binding affinities (**Figure 4**). Moreover, based on the kinetic analysis, the molecular basis of the structural recognition of two histone–protein pairs and a mechanism of histone-mediated DNA damage repair were proposed.

### Protein–Cell Interactions

Tao’s group (107) investigated interaction of herceptin (an antibody used as an antitumor drug) and the membrane HER2. In their study, the binding kinetics of herceptin with HER2 were measured in single intact cultured cells and primary cells extracted from breast tumor tissues.



(Caption appears on following page)

**Figure 4** (Figure appears on preceding page)

(a) Heatmap of binding affinities between histone peptides and histone reader proteins. (b) The binding curves of proteins to respective histones (c). Figure adapted with permission from Reference 106. Abbreviation: RU, refractive unit.

The equilibrium dissociation constant was determined and shown to vary among different cell lines. Significantly weaker herceptin–HER2 interaction was observed when using herceptin-resistant cells compared to those obtained using herceptin-sensitive cells. Furthermore, it was demonstrated that the steric hindrance of membrane protein mucin-4 can alter drug-receptor binding. Subsequently, they studied the same interaction except for the conjugation of herceptin with AuNPs (108). It was found that conjugation significantly affects the binding kinetic and that the mechanism of herceptin–AuNP binding depends on the conjugation density of herceptin on AuNPs and the expression level of HER2 on the cell membrane.

## OTHER APPLICATIONS

Cheng et al. (109) used a prism-based SPR imaging platform to monitor the effect of chemical agents on amyloid- $\beta$  (A $\beta$ ) fibril elongation. A $\beta$  monomers were incubated with Fe<sup>3+</sup>, Cu<sup>2+</sup>, and Zn<sup>2+</sup> (known to promote A $\beta$  fibril growth). In addition, (–)-epigallocatechin gallate (EGCG) (known to inhibit A $\beta$  fibril growth) and the fibrils were covalently attached to the sensor surface. A $\beta$  monomers were then introduced, and the process of fibril elongation was monitored. It was demonstrated that the elongation process was modulated by the presence of metals and EGCG.

The process of toehold-mediated DNA strand displacement was studied using dark-field SPR microscopy and a plasmon ruler (110). The plasmon ruler used was a core-satellite AuNP assembly composed of several satellite nanoparticles bound to a core nanoparticle via DNA hybridization. DNA-strand displacement was triggered by an invader sequence (miRNA-21 oncogen) that released the satellite from the core. The kinetics of strand displacement was investigated for different toehold sequence lengths and homo-/hetero-DNA/RNA duplexes. Apparent rate constants were calculated from the probability of strand displacement. A plasmon ruler was also used for monitoring the extension process of DNA (telomerase primer) activated by a telomerase by Qian et al. (111). AgNPs dimers used as plasmon rulers were created via hybridization of AgNPs functionalized with complementary thiol-terminated DNA. AgNPs dimers were adsorbed on a glass substrate and cell extract, and deoxyribonucleotide triphosphates (dNTPs) were added to allow cellular telomerase to incorporate dNTPs to the end of the telomerase primer. The extended telomerase primer hybridizes with a DNA and forms a rigid structure that results in increasing the distance between AgNPs. Interparticle distance was determined from TEM images. Based on both spectral analysis and dark-field microscopy images, it was demonstrated that telomerases extracted from different cell lines exhibit different activity (i.e., DNA extension rate) and that the telomerase inhibitor EGCG indeed reduces the telomerase activity.

Jia et al. (112) used prism-based SPR imaging for DNA aptamer screening and real-time monitoring of the SELEX process. A target protein, lactoferrin, and a mixture of control proteins were covalently attached to the SPR chip via amine coupling. A DNA library was designed, and the respective DNA sequences were coupled with complementary DNA on AgNPs to create a DNA–AgNP library. In the reported experiments, DNA–AgNPs were flowed along the surface with immobilized lactoferrin and control proteins. Subsequently, the channel with target protein was disconnected and eluted, and the respective DNA was amplified by PCR and used in the following cycle. Finally, specific DNA was sequenced, and aptamer candidates were identified.

The SPR imaging based on a nanohole array was used for nucleic acid sequencing by Cetin et al. (113). They used a nanohole array to which primed-template DNA was attached. This methodology exploits the specificity with which a complex is formed between a primed-template DNA, a dNTP, and a polymerase. A model DNA (4 bp) was sequenced in this work.

SPR microscopy was also used to image and measure the length of a single DNA (114). Yu et al. functionalized a gold surface with amine-terminated thiols over which  $\lambda$ -DNA molecules were stretched by the capillary force. The SPR images were used to determine the average length of the whole  $\lambda$ -DNA and it was found to agree well with theoretical simulations and fluorescence images.

Corn's group (115, 116) investigated the uptake of small molecules (melitin) and large molecules (concanavalin) by hydrogel NPs for the controlled uptake and release of bioactive molecules in drug delivery. They loaded hydrogel NPs with different concentrations of molecules and adsorbed them on the surface of an SPR chip modified with hydrophobic alkanethiols. The difference in the sensor response to loaded and unloaded nanoparticles was found to correlate with the amount of loaded molecules.

## DISCUSSION

The development of optical platforms for SPR imaging and microscopy has been driven by different needs and applications. Whereas in SPR microscopy, research into optical platforms has been concentrated mainly on achieving the best spatial resolution, research in SPR imaging has encompassed activities toward improving performance (both spatial resolution and RI resolution) as well as reducing the size and complexity of SPR imaging devices. RI resolution is one of the main characteristics that describes sensing performance of SPR imaging platforms. However, one should keep in mind that RI resolution (*a*) depends on multiple factors (e.g., spatial and temporal averaging of sensor response) that are often different (or not stated) in different reports and (*b*) is not the best characteristic when comparing platforms employing different surface plasmon modes (i.e., different surface plasmon modes may exhibit rather different electromagnetic field profiles). RI resolutions reported in the literature span a broad range of values ( $10^{-3}$  to  $10^{-7}$ ). The best laboratory SPR imaging platforms achieve an RI resolution of around  $10^{-7}$  while being able to simultaneously measure  $\sim 100$  sensing spots with a temporal resolution of  $\sim 1$  s. In contrast, the performance of compact SPR imaging systems (often based on collinear optics and plasmonic nanostructures) is inferior, typically achieving RI resolutions on the order of  $10^{-3}$ – $10^{-6}$ . When assessing the potential of such devices for bioanalytical applications, it also remains to be seen to what extent miniaturization can be achieved while providing robust and stable optical systems insensitive to environmental factors (e.g., temperature variations), which are often sources of sensor response drifts. Although improving spatial resolution in SPR microscopy has clearly been the main motivation for a large number of research studies, it should be noted that the spatial resolutions reported by different groups were often determined under specific (and different) conditions, making direct comparison difficult. However, it should be noted that several approaches have been developed that allow SPR microscopy platforms to achieve a diffraction-limited resolution ( $\sim 200$  nm). Moreover, SPR microscopy employing advanced image processing methods has been shown to be capable of visualizing the transport of biological objects (organelles) moving inside a cell with high precision (5 nm).

Biosensors based on SPR imaging have been applied in the detection of a broad variety of biologically relevant analytes, ranging from proteins and nucleic acids to viruses and bacteria. Detection performance is typically expressed in terms of the LOD. However, the reported LODs are often determined by different methods that make direct comparison difficult even when the

same analyte is to be detected. Comparison of the detection capabilities of different biosensors for different applications is even more elusive, as the ultimate detection performance of an SPR biosensor depends on multiple factors. These include the performance of the SPR instrument (optical platform, microfluidic system, and functional coating), the detection format, and composition of the sample (although most reports are concerned with the detection in buffer, the number of applications in real-world biological media is growing). Proteins represent the group of analytes targeted most frequently. The LODs achieved in buffer are typically in the pg/mL to ng/mL range; the LODs in complex samples (e.g., blood serum and plasma) are typically higher by an order of magnitude or more. Functional metal NPs are often employed to improve the specificity and LOD of the assay, which is more efficient in combination with the platforms that used surface plasmons with higher penetration depths (e.g., PSPs). Detection of nucleic acids has also been pursued, and the reported LODs are typically in the nM range or in the fM to pM range for direct and particle-enhanced sandwich assays, respectively. The SPR imaging technique has also been shown capable of detecting individual bioparticles. Moreover, SPR imaging platforms have been applied to high-throughput analyses of a multitude of biomolecular interactions, such as small drug–protein receptor, protein–nucleic acid, and protein–protein interactions. SPR imaging and microscopy methods have also been introduced in cell research to provide a platform for the study of individual cells as well as their groups and assemblies. This included investigation of the properties of intact living cells, such as their adhesion, response to external stimuli, signaling, and secretion as well as the interaction of ligands with membrane receptors embedded in the native environment of the cell. The concept of monitoring the interactions involving individual cells has been demonstrated, and SPR microscopy has been shown to provide resolution that allows tracking the individual subcellular structures (organelles, cytoskeleton).

## OUTLOOK

Since their conception, SPR imaging and microscopy have made great advances in terms of both technology and applications. However, they have not yet reached the level of maturity and use of conventional SPR biosensors. Only a few SPR imaging and microscopy commercial platforms are available, which limits the development of new applications and the impact of this technology. This also contributes to a lack of standardization of instrumentation and measurement methodologies that need to be improved in the future. Although the LODs achieved by SPR imaging platforms meet the requirements of numerous relevant bioanalytical applications, analysis of complex samples (e.g., bodily fluids) with minimum or no sample preparation remains a challenge. In the future, this issue is expected to be alleviated by advances in the development of functional coatings and detection methodologies. The need for more sensitive and accurate SPR imaging and microscopy platforms may be addressed by new developments in plasmonics and optical measurement methods. Plasmonic nanostructures may play an important role in some future applications, but their routine use will require the development of cost-effective methods for their fabrication. Given the growing number of applications and complexity of problems addressed by SPR imaging and microscopy, these methods will undoubtedly continue to evolve and have an increasing impact on the fields of biology, medicine, food safety, and security.

## DISCLOSURE STATEMENT

The authors are not aware of any affiliations, memberships, funding, or financial holdings that might be perceived as affecting the objectivity of this review.

## ACKNOWLEDGMENT

This work was supported by the Czech Science Foundation under contract #P205/12/G118.

## LITERATURE CITED

1. Nirschl M, Reuter F, Voros J. 2011. Review of transducer principles for label-free biomolecular interaction analysis. *Biosensors* 1:70–92
2. Gordon JG, Ernst S. 1980. Surface-plasmons as a probe of the electrochemical interface. *Surf. Sci.* 101:499–506
3. Nylander C, Liedberg B, Lind T. 1982. Gas-detection by means of surface-plasmon resonance. *Sens. Actuators* 3:79–88
4. Löfås S, Malmqvist M, Rönnerberg I, Stenberg E, Liedberg B, Lundström I. 1991. Bioanalysis with surface-plasmon resonance. *Sens. Actuators B* 5:79–84
5. Yeatman E, Ash EA. 1987. Surface-plasmon microscopy. *Electron. Lett.* 23:1091–92
6. Rothenhäusler B, Knoll W. 1988. Surface-plasmon microscopy. *Nature* 332:615–17
7. Zeng YJ, Hu R, Wang L, Gu DY, He JN, et al. 2017. Recent advances in surface plasmon resonance imaging: detection speed, sensitivity, and portability. *Nanophotonics* 6:1017–30
8. Wong CL, Olivo M. 2014. Surface plasmon resonance imaging sensors: a review. *Plasmonics* 9:809–24
9. Abbas A, Linman MJ, Cheng Q. 2011. New trends in instrumental design for surface plasmon resonance-based biosensors. *Biosens. Bioelectron.* 26:1815–24
10. D'Agata R, Spoto G. 2013. Surface plasmon resonance imaging for nucleic acid detection. *Anal. Bioanal. Chem.* 405:573–84
11. Liu CJ, Hu FC, Yang W, Xu JY, Chen Y. 2017. A critical review of advances in surface plasmon resonance imaging sensitivity. *Trends Anal. Chem.* 97:354–62
12. Puiu M, Bala C. 2016. SPR and SPR imaging: recent trends in developing nanodevices for detection and real-time monitoring of biomolecular events. *Sensors* 16:870
13. Scarano S, Mascini M, Turner APF, Minunni M. 2010. Surface plasmon resonance imaging for affinity-based biosensors. *Biosens. Bioelectron.* 25:957–66
14. Maier SA. 2007. *Plasmonics: Fundamentals and Applications*. Berlin/Heidelberg: Springer Sci. & Bus. Media
15. Homola J. 2006. *Surface Plasmon Resonance Based Sensors*. Berlin/Heidelberg: Springer
16. Špačková B, Wróbel P, Bocková M, Homola J. 2016. Optical biosensors based on plasmonic nanostructures: a review. *Proc. IEEE* 104:2380–408
17. Berini P. 2009. Long-range surface plasmon polaritons. *Adv. Opt. Photon.* 1:484–588
18. Vecchi G, Giannini V, Rivas JG. 2009. Surface modes in plasmonic crystals induced by diffractive coupling of nanoantennas. *Phys. Rev. B* 80:201401
19. Li XK, Soler M, Ozdemir CI, Belushkin A, Yesilkoy F, Altug H. 2017. Plasmonic nanohole array biosensor for label-free and real-time analysis of live cell secretion. *Lab Chip* 17:2208–17
20. Guo H, Guo JP. 2015. Hybrid plasmon photonic crystal resonance grating for integrated spectrometer biosensor. *Opt. Lett.* 40:249–52
21. Seiler ST, Rich IS, Lindquist NC. 2016. Direct spectral imaging of plasmonic nanohole arrays for real-time sensing. *Nanotechnology* 27:184001
22. Rampazzi S, Danese G, Leporati F, Marabelli F. 2016. A localized surface plasmon resonance-based portable instrument for quick on-site biomolecular detection. *IEEE Trans. Instrum. Meas.* 65:317–27
23. Schasfoort RBM. 2017. Examples of SPR imaging instruments. In *Handbook of Surface Plasmon Resonance*, ed. RBM Schasfoort, pp. 89–97. Cambridge, UK: R. Soc. Chem. 2nd ed.
24. Corso AJ, Zuccon S, Zuppella P, Pelizzo MG. 2015. Flexible SPR system able to switch between Kretschmann and SPRi. *Proc. SPIE 9506*, Opt. Sens., 95061D. <https://doi.org/10.1117/12.2181223>
25. Shao YH, Li Y, Gu DY, Zhang K, Qu JL, et al. 2013. Wavelength-multiplexing phase-sensitive surface plasmon imaging sensor. *Opt. Lett.* 38:1370–72
26. Zeng YJ, Wang L, Wu SY, He JA, Qu JL, et al. 2017. Wavelength-scanning SPR imaging sensors based on an acousto-optic tunable filter and a white light laser. *Sensors* 17:90

27. Laplatine L, Leroy L, Calemczuk R, Baganizi D, Marche PN, et al. 2014. Spatial resolution in prism-based surface plasmon resonance microscopy. *Opt. Expr.* 22:22771–85
28. Bottazzi B, Fornasari L, Frangolho A, Giudicatti S, Mantovani A, et al. 2014. Multiplexed label-free optical biosensor for medical diagnostics. *J. Biomed. Opt.* 19:017006
29. Gomez-Cruz J, Nair S, Manjarrez-Hernandez A, Gavilanes-Parra S, Ascanio G, Escobedo C. 2018. Cost-effective flow-through nanohole array-based biosensing platform for the label-free detection of uropathogenic *E. coli* in real time. *Biosens. Bioelectron.* 106:105–10
30. Guner H, Ozgur E, Kokturk G, Celik M, Esen E, et al. 2017. A smartphone based surface plasmon resonance imaging (SPRi) platform for on-site biodetection. *Sens. Actuators B* 239:571–77
31. Lee KL, You ML, Tsai CH, Lin EH, Hsieh SY, et al. 2016. Nanoplasmonic biochips for rapid label-free detection of imidacloprid pesticides with a smartphone. *Biosens. Bioelectron.* 75:88–95
32. Cappi G, Spiga FM, Moncada Y, Ferretti A, Beyeler M, et al. 2015. Label-free detection of tobramycin in serum by transmission-localized surface plasmon resonance. *Anal. Chem.* 87:5278–85
33. Ruemmele JA, Hall WP, Ruvuna LK, Van Duyne RP. 2013. A localized surface plasmon resonance imaging instrument for multiplexed biosensing. *Anal. Chem.* 85:4560–66
34. Lee KL, Tsai JT, Chih MJ, Yao YD, Wei PK. 2013. High-throughput label-free detection using a gold nanoslit array with 2-D spectral images and spectral integration methods. *IEEE J. Sel. Top. Quantum Electron.* 19. <https://doi.org/10.1109/JSTQE.2012.2234444>
35. Banville FA, Moreau J, Sarkar M, Besbes M, Canva M, Charette PG. 2018. Spatial resolution versus contrast trade-off enhancement in high-resolution surface plasmon resonance imaging (SPRi) by metal surface nanostructure design. *Opt. Expr.* 26:10616–30
36. Banville FA, Söllradl T, Zermatten PJ, Grandbois M, Charette PG. 2015. Improved resolution in SPR and MCWG microscopy by combining images acquired with distinct mode propagation directions. *Opt. Lett.* 40:1165–68
37. Son T, Lee C, Seo J, Choi IH, Kim D. 2018. Surface plasmon microscopy by spatial light switching for label-free imaging with enhanced resolution. *Opt. Lett.* 43:959–62
38. Tan HM, Pechprasarn S, Zhang J, Pitter MC, Somekh MG. 2016. High resolution quantitative angle-scanning widefield surface plasmon microscopy. *Sci. Rep.* 6:20195
39. Watanabe K, Matsuura K, Kawata F, Nagata K, Ning J, Kano H. 2012. Scanning and non-scanning surface plasmon microscopy to observe cell adhesion sites. *Biomed. Opt. Expr.* 3:354–59
40. Berguiga L, Streppa L, Boyer-Provera E, Martinez-Torres C, Schaeffer L, et al. 2016. Time-lapse scanning surface plasmon microscopy of living adherent cells with a radially polarized beam. *Appl. Opt.* 55:1216–27
41. Mandracchia B, Pagliarulo V, Paturzo M, Ferraro P. 2016. Through-the-objective holographic surface plasmon resonance imaging for quantitative measurement of thin film thickness. *Proc. SPIE* 9718, Quant. Phase Imaging 2, 97182W. <https://doi.org/10.1117/12.2218419>
42. Zhang J, Dai S, Ma C, Di J, Zhao J. 2017. Common-path digital holographic microscopy for near-field phase imaging based on surface plasmon resonance. *Appl. Opt.* 56:3223–28
43. Zhang J, Dai S, Ma C, Di J, Zhao J. 2017. Compact surface plasmon holographic microscopy for near-field film mapping. *Opt. Lett.* 42:3462–65
44. Gao YK, Xin ZM, Gan QQ, Cheng XH, Bartoli FJ. 2013. Plasmonic interferometers for label-free multiplexed sensing. *Opt. Expr.* 21:5859–71
45. Chen PY, Chung MT, McHugh W, Nidetz R, Li YW, et al. 2015. Multiplex serum cytokine immunoassay using nanoplasmonic biosensor microarrays. *ACS Nano* 9:4173–81
46. Soler M, Belushkin A, Cavallini A, Kebbi-Beghdadi C, Greub G, Altug H. 2017. Multiplexed nanoplasmonic biosensor for one-step simultaneous detection of *Chlamydia trachomatis* and *Neisseria gonorrhoeae* in urine. *Biosens. Bioelectron.* 94:560–67
47. Liu XJ, Zhang QQ, Tu Y, Zhao WF, Gai HW. 2013. Single gold nanoparticle localized surface plasmon resonance spectral imaging for quantifying binding constant of carbohydrate-protein interaction. *Anal. Chem.* 85:11851–57
48. Schasfoort RBM. 2017. *Handbook of Surface Plasmon Resonance*. Cambridge, UK: R. Soc. Chem. 2nd ed.



49. Romanov V, Davidoff SN, Miles AR, Grainger DW, Gale BK, Brooks BD. 2014. A critical comparison of protein microarray fabrication technologies. *Analyst* 139:1303–26
50. Vaisocherova H, Brynda E, Homola J. 2015. Functionalizable low-fouling coatings for label-free biosensing in complex biological media: advances and applications. *Anal. Bioanal. Chem.* 407:3927–53
51. Syal K, Iriya R, Yang YZ, Yu H, Wang SP, et al. 2016. Antimicrobial susceptibility test with plasmonic imaging and tracking of single bacterial motions on nanometer scale. *ACS Nano* 10:845–52
52. Bulard E, Bouchet-Spinelli A, Chaud P, Roget A, Calemczuk R, et al. 2015. Carbohydrates as new probes for the identification of closely related *Escherichia coli* strains using surface plasmon resonance imaging. *Anal. Chem.* 87:1804–11
53. Simon L, Lautner G, Gyurcsanyi RE. 2015. Reliable microspotting methodology for peptide-nucleic acid layers with high hybridization efficiency on gold SPR imaging chips. *Anal. Methods* 7:6077–82
54. Nand A, Singh V, Perez JB, Tyagi D, Cheng ZQ, Zhu JS. 2014. *In situ* protein microarrays capable of real-time kinetics analysis based on surface plasmon resonance imaging. *Anal. Biochem.* 464:30–35
55. Manuel G, Lupták A, Corn RM. 2016. A microwell-printing fabrication strategy for the on-chip templated biosynthesis of protein microarrays for surface plasmon resonance imaging. *J. Phys. Chem. C* 120:20984–90
56. Kruis IC, Lowik D, Boelens WC, van Hest JCM, Puijn GJM. 2016. An integrated, peptide-based approach to site-specific protein immobilization for detection of biomolecular interactions. *Analyst* 141:5321–28
57. Wood JB, Szyndler MW, Halpern AR, Cho K, Corn RM. 2013. Fabrication of DNA microarrays on polydopamine-modified gold thin films for SPR imaging measurements. *Langmuir* 29:10868–73
58. Belushkin A, Yesilkoy F, Altug H. 2018. Nanoparticle-enhanced plasmonic biosensor for digital biomarker detection in a microarray. *ACS Nano* 12:4453–61
59. Escobedo C, Chou YW, Rahman M, Duan XB, Gordon R, et al. 2013. Quantification of ovarian cancer markers with integrated microfluidic concentration gradient and imaging nanohole surface plasmon resonance. *Analyst* 138:1450–58
60. Hu WH, Chen HM, Shi ZZ, Yu L. 2014. Dual signal amplification of surface plasmon resonance imaging for sensitive immunoassay of tumor marker. *Anal. Biochem.* 453:16–21
61. Hu WH, He GL, Zhang HH, Wu XS, Li JL, et al. 2014. Polydopamine-functionalization of graphene oxide to enable dual signal amplification for sensitive surface plasmon resonance imaging detection of biomarker. *Anal. Chem.* 86:4488–93
62. Liu CJ, Wang X, Xu JY, Chen Y. 2016. Chemical strategy to stepwise amplification of signals in surface plasmon resonance imaging detection of saccharides and glycoconjugates. *Anal. Chem.* 88:10011–18
63. Monteiro JP, Predabon SM, Bonafé EG, Martins AF, Brolo AG, et al. 2017. SPR platform based on image acquisition for HER2 antigen detection. *Nanotechnology* 28. <https://doi.org/10.1088/1361-6528/28/4/045206>
64. Gorodkiewicz E, Sienczyk M, Regulska E, Grzywa R, Pietrusiewicz E, et al. 2012. Surface plasmon resonance imaging biosensor for cathepsin G based on a potent inhibitor: Development and applications. *Anal. Biochem.* 423:218–23
65. Grzywa R, Gorodkiewicz E, Burchacka E, Lesner A, Laudanski P, et al. 2014. Determination of cathepsin G in endometrial tissue using a surface plasmon resonance imaging biosensor with tailored phosphonic inhibitor. *Eur. J. Obstet. Gynecol. Reprod. Biol.* 182:38–42
66. Sankiewicz A, Romanowicz L, Laudanski P, Zelazowska-Rutkowska B, Puzan B, et al. 2016. SPR imaging biosensor for determination of laminin-5 as a potential cancer marker in biological material. *Anal. Bioanal. Chem.* 408:5269–76
67. Sankiewicz A, Lukaszewski Z, Trojanowska K, Gorodkiewicz E. 2016. Determination of collagen type IV by Surface Plasmon Resonance Imaging using a specific biosensor. *Anal. Biochem.* 515:40–46
68. Tokarzewicz A, Romanowicz L, Sveklo I, Gorodkiewicz E. 2016. The development of a matrix metalloproteinase-1 biosensor based on the surface plasmon resonance imaging technique. *Anal. Methods* 8:6428–35

69. Hendriks J, Stojanovic I, Schasfoort RBM, Saris DBF, Kaiperien M. 2018. Nanoparticle enhancement cascade for sensitive multiplex measurements of biomarkers in complex fluids with surface plasmon resonance imaging. *Anal. Chem.* 90:6563–71
70. Oh BR, Chen P, Nidetz R, McHugh W, Fu J, et al. 2016. Multiplexed nanoplasmonic temporal profiling of T-cell response under immunomodulatory agent exposure. *ACS Sens.* 1:941–48
71. Rosman C, Prasad J, Neiser A, Henkel A, Edgar J, Sonnichsen C. 2013. Multiplexed plasmon sensor for rapid label-free analyte detection. *Nano Lett.* 13:3243–47
72. Hu FC, Xu JY, Chen Y. 2017. Surface plasmon resonance imaging detection of sub-femtomolar microRNA. *Anal. Chem.* 89:10071–77
73. Vaisocherová H, Šipová H, Visová I, Bocková M, Springer T, et al. 2015. Rapid and sensitive detection of multiple microRNAs in cell lysate by low-fouling surface plasmon resonance biosensor. *Biosens. Bioelectron.* 70:226–31
74. Mariani S, Ermini ML, Scarano S, Bellissima F, Bonini M, et al. 2013. Improving surface plasmon resonance imaging of DNA by creating new gold and silver based surface nanostructures. *Microchim. Acta* 180:1093–99
75. Wu JL, Huang Y, Bian XT, Li DD, Cheng Q, Ding SJ. 2016. Biosensing of BCR/ABL fusion gene using an intensity-interrogation surface plasmon resonance imaging system. *Opt. Commun.* 377:24–32
76. Foudeh AM, Daoud JT, Faucher SP, Veres T, Tabrizian M. 2014. Sub-femtomole detection of 16s rRNA from *Legionella pneumophila* using surface plasmon resonance imaging. *Biosens. Bioelectron.* 52:129–35
77. Melaine F, Tabrizian M. 2016. Functionalized gold nanoparticles for surface plasmon resonance detection of *Legionella pneumophila* 16s rRNA. *IEEE Sens.* <https://doi.org/10.1109/ICSENS.2016.7808696>
78. Melaine F, Saad M, Faucher S, Tabrizian M. 2017. Selective and high dynamic range assay format for multiplex detection of pathogenic *Pseudomonas aeruginosa*, *Salmonella typhimurium*, and *Legionella pneumophila* RNAs using surface plasmon resonance imaging. *Anal. Chem.* 89:7802–7
79. Aura AM, D'Agata R, Spoto G. 2017. Ultrasensitive detection of *Staphylococcus aureus* and *Listeria monocytogenes* genomic DNA by nanoparticle-enhanced surface plasmon resonance imaging. *Chem. Select* 2:7024–30
80. Bouguelia S, Roupioz Y, Slimani S, Mondani L, Casabona MG, et al. 2013. On-chip microbial culture for the specific detection of very low levels of bacteria. *Lab Chip* 13:4024–32
81. Mondani L, Roupioz Y, Delannoy S, Fach P, Livache T. 2014. Simultaneous enrichment and optical detection of low levels of stressed *Escherichia coli* O157:H7 in food matrices. *J. Appl. Microbiol.* 117:537–46
82. Morlay A, Piat F, Mercey T, Roupioz Y. 2016. Immunological detection of *Cronobacter* and *Salmonella* in powdered infant formula by plasmonic label-free assay. *Lett. Appl. Microbiol.* 62:459–65
83. Yodmongkol S, Thaweboon S, Thaweboon B, Puttharugsa C, Sutapun B, et al. 2016. Application of surface plasmon resonance biosensor for the detection of *Candida albicans*. *Jpn. J. Appl. Phys.* 55:02BE03
84. Shpacovitch V, Temchura V, Matrosovich M, Hamacher J, Skolnik J, et al. 2015. Application of surface plasmon resonance imaging technique for the detection of single spherical biological submicrometer particles. *Anal. Biochem.* 486:62–69
85. Zhu L, Wang K, Cui J, Liu H, Bu XL, et al. 2014. Label-free quantitative detection of tumor-derived exosomes through surface plasmon resonance imaging. *Anal. Chem.* 86:8857–64
86. Syal K, Wang W, Shan XN, Wang SP, Chen HY, Tao NJ. 2015. Plasmonic imaging of protein interactions with single bacterial cells. *Biosens. Bioelectron.* 63:131–37
87. Abadian PN, Tandogan N, Jamieson JJ, Goluch ED. 2014. Using surface plasmon resonance imaging to study bacterial biofilms. *Biomicrofluidics* 8:021804
88. Abadian PN, Goluch ED. 2015. Surface plasmon resonance imaging (SPRi) for multiplexed evaluation of bacterial adhesion onto surface coatings. *Anal. Methods* 7:115–22
89. Malleve F, Templier V, Mathey R, Leroy L, Roupioz Y, et al. 2016. Real-time toxicity testing of silver nanoparticles to *Salmonella* Enteritidis using surface plasmon resonance imaging: a proof of concept. *NanoImpact* 1:55–59

90. Streppa L, Berguiga L, Provera EB, Ratti F, Goillot E, et al. 2016. Tracking in real time the crawling dynamics of adherent living cells with a high resolution surface plasmon microscope. *Proc. SPIE* 9724, Plasm. Biol. Med. 13, 97240G. <https://doi.org/10.1117/12.2211331>
91. Tu L, Li XZ, Bian ST, Yu YT, Li JX, et al. 2017. Label-free and real-time monitoring of single cell attachment on template-stripped plasmonic nano-holes. *Sci. Rep.* 7:11020
92. Yang YZ, Yu H, Shan XN, Wang W, Liu XW, et al. 2015. Label-free tracking of single organelle transportation in cells with nanometer precision using a plasmonic imaging technique. *Small* 11:2878–84
93. Shinohara H, Sakai Y, Mir TA. 2013. Real-time monitoring of intracellular signal transduction in PC12 cells by two-dimensional surface plasmon resonance imager. *Anal. Biochem.* 441:185–89
94. Mir TA, Shinohara H. 2013. Two-dimensional surface plasmon resonance imager: an approach to study neuronal differentiation. *Anal. Biochem.* 443:46–51
95. Zhang LL, Chen X, Wei HT, Li H, Sun JH, et al. 2014. Development of dual-channel surface plasmon resonance imaging system applied to living tumour cell analyses. *IET Micro Nano Lett.* 9:382–85
96. Zhang LL, Chen X, Du Y, Zhang Q, Li H, et al. 2015. A surface plasmon resonance imaging system for the stimulated living cell analysis. *Optoelectron. Lett.* 11:77–80
97. Zhang FN, Wang SP, Yin LL, Yang YZ, Guan Y, et al. 2015. Quantification of epidermal growth factor receptor expression level and binding kinetics on cell surfaces by surface plasmon resonance imaging. *Anal. Chem.* 87:9960–65
98. Xiong B, Huang ZR, Zou HY, Qiao CY, He Y, Yeung ES. 2017. Single plasmonic nanosprings for visualizing reactive-oxygen-species-activated localized mechanical force transduction in live cells. *ACS Nano* 11:541–48
99. Berthuy OI, Blum LJ, Marquette CA. 2016. Cancer-cells on chip for label-free detection of secreted molecules. *Biosensors* 6:2
100. Raghu D, Christodoulides JA, Delehanty JB, Byers JM, Raphael MP. 2015. A label-free technique for the spatio-temporal imaging of single cell secretions. *J. Vis. Exp.* 105:53120
101. Li SP, Yang M, Zhou WF, Johnston TG, Wang R, Zhu JS. 2015. Dextran hydrogel coated surface plasmon resonance imaging (SPRi) sensor for sensitive and label-free detection of small molecule drugs. *Appl. Surf. Sci.* 355:570–76
102. Zhou WF, Yang M, Li SP, Zhu JS. 2018. Surface plasmon resonance imaging validation of small molecule drugs binding on target protein microarrays. *Appl. Surf. Sci.* 450:328–35
103. Pillet F, Sanchez A, Formosa C, Séverac M, Trévisiol E, et al. 2013. Dendrimer functionalization of gold surface improves the measurement of protein-DNA interactions by surface plasmon resonance imaging. *Biosens. Bioelectron.* 43:148–54
104. Rubio MJ, Svobodová M, Mairal T, O'Sullivan CK. 2016. Surface plasmon resonance imaging (SPRi) for analysis of DNA aptamer:  $\beta$ -conglutinin interactions. *Methods* 97:20–26
105. Miyachi K, Wakao M, Suda Y. 2015. Syntheses of chondroitin sulfate tetrasaccharide structures containing 4,6-disulfate patterns and analysis of their interaction with glycosaminoglycan-binding protein. *Bioorg. Med. Chem. Lett.* 25:1552–55
106. Zhao S, Yang M, Zhou WF, Zhang BC, Cheng ZQ, et al. 2017. Kinetic and high-throughput profiling of epigenetic interactions by 3D-carbene chip-based surface plasmon resonance imaging technology. *PNAS* 114:E7245–54
107. Wang W, Yin LL, Gonzalez-Malerva L, Wang SP, Yu XB, et al. 2014. *In situ* drug-receptor binding kinetics in single cells: a quantitative label-free study of anti-tumor drug resistance. *Sci. Rep.* 4:6609
108. Yin LL, Yang YZ, Wang SP, Wang W, Zhang ST, Tao NJ. 2015. Measuring binding kinetics of antibody-conjugated gold nanoparticles with intact cells. *Small* 11:3782–88
109. Cheng XR, Hau BYH, Veloso AJ, Martic S, Kraatz HB, Kerman K. 2013. Surface plasmon resonance imaging of amyloid- $\beta$  aggregation kinetics in the presence of epigallocatechin gallate and metals. *Anal. Chem.* 85:2049–55
110. Li MX, Xu CH, Zhang N, Qian GS, Zhao W, et al. 2018. Exploration of the kinetics of toehold mediated strand displacement via plasmon rulers. *ACS Nano* 12:3341–50
111. Qian GS, Zhang TT, Zhao W, Xu JJ, Chen HY. 2017. Single-molecule imaging of telomerase activity via linear plasmon rulers. *Chem. Commun.* 53:4710–13

112. Jia WC, Li H, Wilkop T, Liu XH, Yu XD, et al. 2018. Silver decahedral nanoparticles empowered SPR imaging-SELEX for high throughput screening of aptamers with real-time assessment. *Biosens. Bioelectron.* 109:206–13
113. Cetin AE, Iyidogan P, Hayashi Y, Wallen M, Vijayan K, et al. 2018. Plasmonic sensor could enable label-free DNA sequencing. *ACS Sens.* 3:561–68
114. Yu H, Shan XN, Wang SP, Chen HY, Tao NJ. 2014. Plasmonic imaging and detection of single DNA molecules. *ACS Nano* 8:3427–33
115. Cho K, Fasoli JB, Yoshimatsu K, Shea KJ, Corn RM. 2015. Measuring melittin uptake into hydrogel nanoparticles with near-infrared single nanoparticle surface plasmon resonance microscopy. *Anal. Chem.* 87:4973–79
116. Maley AM, Terada Y, Onogi S, Shea KJ, Miura Y, Corn RM. 2016. Measuring protein binding to individual hydrogel nanoparticles with single-nanoparticle surface plasmon resonance imaging microscopy. *J. Phys. Chem. C* 120:16843–49